

## Highlights

### **Adaptive Time-step Training for Enhancing Spike-Based Neural Radiance Fields**

Ranxi Lin, Canming Yao, Jiayi Li, Weihang Liu, Xin Lou, Pingqiang Zhou

- The proposed PATA framework enables scene-adaptive time-step training for spike-based NeRF
- Hybrid input mode boosts early time-step contribution, supporting time-step reduction
- Two-phase training with adversarial loss balances rendering quality and efficiency

# Adaptive Time-step Training for Enhancing Spike-Based Neural Radiance Fields

Ranxi Lin<sup>a</sup>, Canming Yao<sup>b</sup>, Jiayi Li<sup>a</sup>, Weihang Liu<sup>a</sup>, Xin Lou<sup>a</sup>, Pingqiang Zhou<sup>a</sup>

<sup>a</sup>*School of Information Science and Technology, ShanghaiTech University, Shanghai, 201203, Shanghai, China*

<sup>b</sup>*Guangdong Institute of Intelligence Science and Technology, Zhuhai, 519031, Guangdong, China*

---

## Abstract

Neural Radiance Fields (NeRF)-based models have achieved remarkable success in 3D reconstruction and rendering tasks. However, during both training and inference, these models rely heavily on dense point sampling along rays from multiple viewpoints, resulting in a surge in floating-point operations and severely limiting their use in resource-constrained scenarios like edge computing. Spiking Neural Networks (SNNs), which communicate via binary spikes over discrete time steps, offer a promising alternative due to their energy-efficient nature. Given the inherent variability in scene scale and texture complexity in neural rendering and the prevailing practice of training separate models per scene, we propose a spike-based NeRF framework with a dynamic time step training strategy, termed Pretrain-Adaptive Time-step Adjustment (PATA). This approach automatically explores the trade-off between rendering quality and time step length during training. Consequently, it enables scene-adaptive inference with variable time steps and reduces the additional consumption of computational resources in the inference process. Anchoring to the established Instant-NGP architecture, we evaluate our method across diverse datasets. The experimental results show that PATA can preserve rendering fidelity while reducing inference time steps by 64% and running power by 61.55%.

*Keywords:*

Spiking Neural Networks, Neural Rendering, Dynamic Time Step, Low-Latency

---

## 1. INTRODUCTION

Neural Radiance Fields (NeRF) [1] has been widely used in various 3D reconstruction and rendering tasks with superior performance. By encoding scene geometry and appearance implicitly through a neural network, NeRF maps 3D coordinates and viewing directions to volumetric density and view-dependent radiance. This representation enables high-fidelity image synthesis from arbitrary viewpoints. However, training NeRF requires dense sampling of points along rays cast from multiple camera poses, leading to extensive computational demands. The predominant use of Multi-Layer Perceptrons (MLPs) [2] further exacerbates this issue, as the network must process a massive number of multiply-accumulate (MAC) operations per sample, resulting in substantial computational load and power consumption [3–5].

While prior work has explored pruning [6, 7] and quantization [8–10] to reduce computational demand during inference, these methods do not fundamentally address the computation and power overhead from extensive multiply-accumulate (MAC) operations. In contrast, Spiking Neural Networks (SNNs) offer a paradigm shift by leveraging event-driven computation and binary spike communication. Unlike conventional Artificial Neural Networks (ANNs), SNNs replace MAC operations with sparse accumulations (AC) [11, 12], and their spiking neurons activate only when membrane potentials exceed a threshold, naturally enforcing activation sparsity. This biologically inspired architecture not only enhances computation and energy efficiency but also enables native processing of spatiotemporal data [13, 14]. Building on these advantages, recent studies have successfully integrated SNNs with NeRF for 3D rendering tasks, demonstrating both high rendering quality and significantly reduced power consumption [4, 15–19].

However, as NeRF trains a model for each independent scene and different scenes exhibit varying geometric and textural complexity, the required model capacity can adapt accordingly [5, 20–22] to reduce computation. In SNN implementations, as demonstrated in Figure 1, we observe a strong positive correlation between rendering quality and the maximum time step  $T$ .

Prior research has demonstrated that increasing the time step ( $T$ ) in SNNs enhances their information capacity [23, 24]. However, existing approaches typically treat  $T$  as a fixed hyperparameter, overlooking its critical relationship with scene complexity [25–27] in the NeRF scenario. While larger  $T$  values improve rendering quality for simple scenes, they unnecessarily increase computational overhead and resource requirements [28, 29].

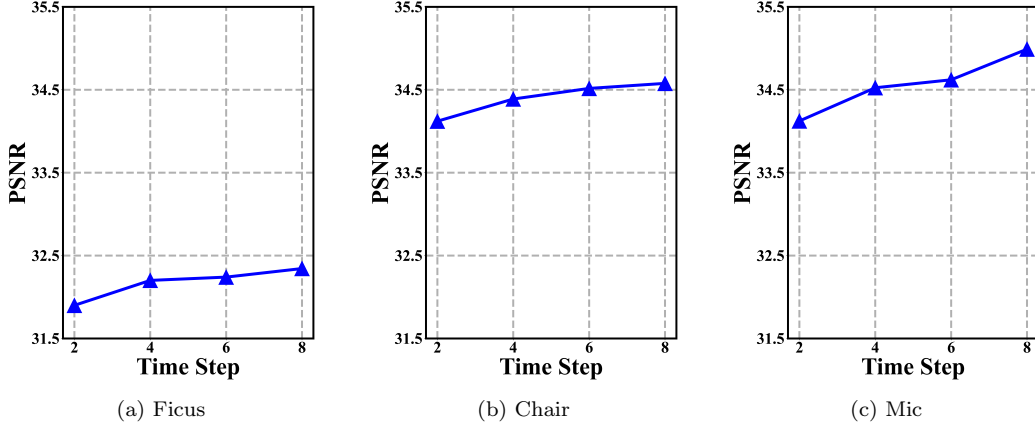


Figure 1: The Peak Signal-to-Noise Ratio (PSNR) improves significantly with increasing time steps in different scenes. Note that for the same PSNR, different time steps are required for various scenarios.

Conversely, insufficient model capacity for complex scenes leads to visual artifacts in rendered outputs. This presents a key challenge: determining scene-adaptive time steps that simultaneously optimize computation/energy efficiency and preserve rendering quality remains an open research question.

This paper proposes a dynamic time-step training strategy for spike-based NeRF models that automatically optimizes the performance-energy trade-off during training. Our framework, named Pretrain-Adapt Time-step Adjustment (PATA), enables scene-adaptive time-step selection during inference by dynamically adjusting time steps based on training loss. Specifically, to increase the contribution of outputs from earlier time steps, we introduce a novel hybrid input mode with different input attenuation strategies at various time steps. In addition, we parameterize the target time step and distinguish it from the maximum time step. During the training process, we utilize adversarial loss to associate the target time step with the scenes, and collaboratively optimize the model’s output at the target time step by using the output at  $T$  time steps as soft labels along with the ground truth. Lastly, to prevent drastic fluctuations in training loss due to changes in the target time step, we propose a smoothing method based on the value of the target time step to ensure training stability.

Our main contributions are summarized as follows:

- **Hybrid Input Mode:** Through rigorous analysis of spiking neuron dynamics across time steps, we develop a novel hybrid input mode



that employs distinct decay strategies for initial versus subsequent time steps. This innovation significantly boosts the influence of early time-step outputs on final results, effectively compensating for performance degradation when reducing temporal resolution.

- **Adaptive Time-Step Training:** We propose a parameterized target time step ( $t_r^*$ ) framework with a two-phase optimization strategy. The first phase establishes a baseline using full time steps ( $T$ ), while the second phase simultaneously optimizes both scene-appropriate time steps and rendering quality through our composite loss function.
- **Substantial Efficiency Gains:** Comprehensive experiments demonstrate our method maintains competitive performance while reducing required inference time steps by 64%, achieving remarkable 61.55% energy savings compared to conventional ANN implementations - a significant advancement in efficient neural rendering.

## 2. RELATED WORK

### 2.1. Neural Rendering Field

Since the introduction of Neural Radiance Fields (NeRF), significant research efforts have been devoted to enhancing its capabilities from multiple perspectives [3, 30–34]. The original NeRF framework revolutionized novel view synthesis by employing a neural network to implicitly encode scene properties, mapping 3D coordinates and viewing directions to volumetric density and view-dependent radiance. This approach achieves photorealistic rendering through differentiable volume rendering. Several notable improvements have been made to the original NeRF architecture. Mip-NeRF [3] addresses aliasing artifacts by introducing multiscale scene representation and conical frustum sampling, significantly improving rendering quality. For computational efficiency, Instant-NGP [32] proposes a hash-based feature grid representation combined with two compact MLPs, dramatically accelerating rendering while maintaining quality. In the domain of model compression, BiRF [30] implements a binary-encoded feature grid through binarization-aware training, achieving substantial memory savings without reducing computational complexity during inference.

## 2.2. Direct Training of SNNs

SNNs typically process information through multiple time steps, requiring efficient information flow across both spatial (layers) and temporal (time steps) dimensions during training and inference. The non-differentiable nature of spiking operations poses a fundamental challenge for gradient-based optimization. To address this, Wu et al.[35] proposed Spatio-Temporal Back-propagation (STBP) with surrogate gradients, which has become a standard training approach for SNNs [36]. Recent advances have focused on two main directions: (1) enhancing neuronal dynamics through modified computational processes [15, 37–40], often at the cost of increased computational overhead; (2) developing specialized loss functions that leverage SNN characteristics to improve training efficiency [41–45], which can not only optimizing network sparsity and architecture [43, 45], but can be achieved without additional computational complexity.

Dynamic time-step adaptation has emerged as another important research direction [46–49]. Li et al.[46] proposed an early-stopping mechanism based on softmax confidence thresholds for classification tasks, though this requires explicit label supervision. Li and Geller [47] introduced a reinforcement learning-based time-step adjustment strategy using an auxiliary policy network. However, these approaches primarily focus on per-sample adaptive inference and face practical limitations: while individual samples may terminate early, the overall batch processing time remains constrained by the longest-running sample, leading to suboptimal throughput improvements.

## 2.3. Spike-based Neural Rendering

Recent advances have demonstrated successful integration of SNNs with NeRF [4, 15–19]. Liao et al. [15] developed a hybrid ANN-SNN architecture with novel spiking neuron dynamics to enable continuous geometric representation. For geometric reconstruction tasks, Gu et al. [18] introduced an innovative polling strategy and designed specialized surrogate gradients. Yao et al. [4] addressed novel view synthesis by mapping ray sampling points to SNN time steps and proposing a TCP scheme to handle variable sampling densities across rays. Wang et al. [17] further enhanced the framework through a grouped spiking neuron mechanism for improved cross-region communication. Compared to these approaches, our solution offers distinct advantages: (1) it maintains the original neuron computational model without additional operations, (2) preserves the input dimensionality, and (3) can be seamlessly integrated with existing spike-based NeRF architectures.

### 3. PRELIMINARIES

#### 3.1. Grid-based Neural Radiance Field

The INGP-NeRF model divides space into multiple grids of different resolutions, assigning indices  $\mathbf{x}$  and feature vectors  $\Phi_\theta$  to the corners of each voxel within these grids, which are then stored in a hash table. For the coordinates of input sample points, linear interpolation is performed based on their relative positions within different hierarchical grids to obtain the feature vectors of the sample points, which are then fed into the density network. For the viewing direction, it is encoded using the Spherical Harmonics (SH) encoder before being fed to the color network:

$$\mathbf{f} = \text{interp}(\mathbf{x}, \Phi_\theta) \quad (1)$$

$$h, \sigma = MLP_{\text{density}}(\mathbf{f}), \mathbf{c} = MLP_{\text{color}}(\mathbf{d}, h) \quad (2)$$

INGP-NeRF employs multiscale occupancy grids to expedite the sampling process. During training, it dynamically labels whether each grid cell is nonempty. At the time of sampling, only nonempty grid cells are sampled, markedly enhancing sampling efficiency. After the aforementioned process has taken place, for the sampled points lying on the same ray  $\mathbf{r}(t) = \mathbf{o} + t\mathbf{d}$ , the RGB value of the ray is calculated using the volume rendering method proposed in [1]:

$$\alpha_i = 1 - \exp(-\sigma_i \delta_i), \quad T_i = \prod_{j=1}^{i-1} (1 - \alpha_j) \quad (3)$$

$$\hat{C}(\mathbf{r}) = \sum_{i=1}^N T_i \alpha_i \mathbf{c}_i \quad (4)$$

Where  $T_i$  represents the transmittance and  $\delta_i = t_{i+1} - t_i$  denotes the distance between adjacent sampled points.

#### 3.2. Neuron Model

The most widely used neuron model in SNNs is currently the Leaky Integrate-and-Fire (LIF) model [50]. The membrane potential update equation is as follows [51]:

$$v^l(t) = \begin{cases} (1 - \frac{1}{\tau})v^l(t-1) + \frac{1}{\tau}i(t), & \text{if decay input;} \\ (1 - \frac{1}{\tau})v^l(t-1) + i(t), & \text{if not decay input;} \end{cases} \quad (5)$$

Where  $i(t) = W^l s^{l-1}(t)$ , with  $s^{l-1}(t)$  representing the output spikes of neurons in the preceding layer at time  $t$ ,  $v^l(t)$  denotes the membrane potential of neurons in the  $l$ -th layer at time  $t$ ,  $\tau$  is the decay factor, which governs the decay amplitude of the membrane potential at each time step. If the decaying input mode is employed, a fraction of the input will undergo decay before accumulating; otherwise, the input will be directly added to the membrane potential. When the membrane potential exceeds the threshold, the LIF neuron will emit a spike and reset. We opt for the soft reset with the calculation carried out as follows:

$$v^l(t) = v^l(t) - s^l(t)\theta^l \quad (6)$$

Where  $s^l(t) = H(v^l(t) - \theta^l)$ , with  $H(\cdot)$  denoting the Heaviside function. Due to the non-differentiability of the Heaviside function, the most widely used solution to enable parameter updating in SNNs using backpropagation algorithms is the surrogate gradient. In our experiments, the surrogate gradient used is as follows:

$$\frac{dH(x)}{dx} = \frac{1}{1 + \exp(-\alpha x)} \quad (7)$$

Where  $\alpha$  is a predefined hyperparameter, and defaults to 4.

## 4. THE PROPOSED METHOD

In this section, we introduce the proposed PATA strategy, which effectively reduces the time steps and energy consumption required for inference while maintaining ANN-level rendering quality. The complete framework, including both the radiance field reconstruction and training procedure, is depicted in Figure 2.

### 4.1. Spike-based Neural Rendering

Figure 2(a) illustrates our spike-based NeRF rendering pipeline. We employ Parametric Leaky Integrate-and-Fire (PLIF) neurons [52] with trainable decay factor  $\tau$  shared within each spiking layer. Following the original NeRF architecture, we first encode input coordinates into high-dimensional features. These features are then processed through modified density and color networks where we replace conventional activation functions with PLIF neurons. To maintain temporal information, we augment both networks with additional PLIF layers that accumulate membrane potentials without spike emission. The resulting outputs ( $\sigma$  for density and  $c$  for color) are fed into the differentiable rendering module to generate radiance predictions.

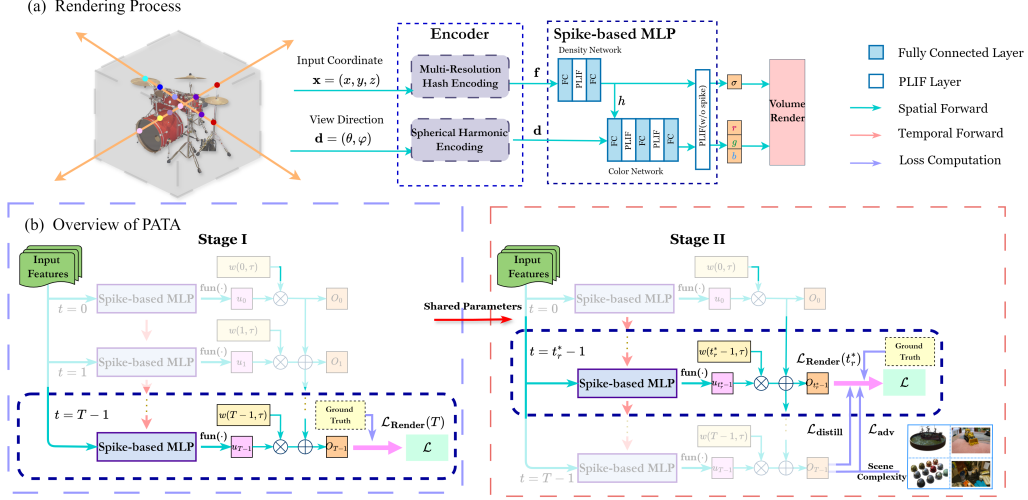


Figure 2: (a) presents the process of rendering. The encoded features are fed into the density and the color network, respectively, and the outputs of the spike-based MLP at the specified time step are used as  $\sigma$  and  $rgb$  for rendering. (b) Overview of the training framework for PATA. In the initial stage, the model is trained by computing  $\mathcal{L}_{\text{Render}}(T)$  based on the output obtained at the maximum time step  $T$ . In the second stage, the model still trains with  $T$  time steps. During this stage, we calculate  $\mathcal{L}_{\text{Render}}(t^*)$  using the output generated at the  $t^*$  time step and compute  $\mathcal{L}_{\text{distill}}$  by employing the output from the  $T$  time step as a soft label. Furthermore, we introduce  $\mathcal{L}_{\text{adv}}$  to establish the connection between the training of  $t^*$  and the scene, and then achieve a trade-off between the length of  $t^*$  and the rendering quality.

#### 4.2. Hybrid Input Mode

Given that our output layer accumulates membrane potentials without spike generation, we formulate the output at time step  $T$  as:

$$O_T = \sum_{t=0}^{T-1} w(t, \tau) \cdot \text{func}(i_t) \quad (8)$$

where  $w(t, \tau)$  represents the contribution weight of time step  $t$  to the final output, and  $\text{func}(\cdot)$  denotes the exponential function for the density network and sigmoid activation for the color network. Notably, the density network processes only the first dimension through the PLIF layer at each time step, while the remaining dimensions serve as hidden features  $\mathbf{h}$  that concatenate with viewing direction features  $\mathbf{d}$  as color network inputs. The weight func-

tion  $w(t, \tau)$  follows distinct formulations depending on the input mode:

$$w(t, \tau) = \begin{cases} (1 - \frac{1}{\tau})^{T-t-1} \frac{1}{\tau}, & \text{if decay input mode} \\ (1 - \frac{1}{\tau})^{T-t-1}, & \text{if non-decay input mode} \end{cases} \quad (9)$$

We observe that both modes exhibit monotonically increasing weights toward later time steps, making the model performance sensitive to time step reduction. To address this, we propose a hybrid input scheme that strategically combines both modes:

$$v^l(t) = \begin{cases} i(t), & \text{if } t = 0 \\ (1 - \frac{1}{\tau})v^l(t-1) + \frac{1}{\tau}i(t), & \text{if } t > 0 \end{cases} \quad (10)$$

This hybrid approach modifies the weight function as:

$$w(t, \tau) = \begin{cases} (1 - \frac{1}{\tau})^{T-t-1}, & \text{if } t = 0 \\ (1 - \frac{1}{\tau})^{T-t-1} \frac{1}{\tau}, & \text{if } t > 0 \end{cases} \quad (11)$$

Crucially, this formulation maintains  $\sum_{t=0}^{T-1} w(t, \tau) = 1$  for all  $\tau > 1$ . As demonstrated in Figure 3, our hybrid mode significantly boosts the contribution of the initial time step while suppressing later time steps through appropriate  $\tau$  selection. This mechanism enables effective time step reduction without compromising model performance.

### 4.3. Pretrain-Adapt Time-step Adjustment

#### 4.3.1. Overall Framework

Our framework enables dynamic time-step adaptation by parameterizing the target time step  $t^*$  as a learnable variable, distinct from the fixed maximum time step  $T$ . To the best of our knowledge, this is the first work to include the timestep as a trainable parameter. The continuous-valued  $t^*$  is quantized to discrete time steps through:

$$t_r^* = \text{Round}(\text{Clamp}(t^*, \min = 1, \max = T)) \quad (12)$$

where  $\text{Round}(\cdot)$  performs nearest-integer rounding and  $\text{Clamp}(\cdot)$  maintains valid time-step bounds.

Direct optimization of  $t^*$  faces two challenges: training instability during early iterations when model representations are underdeveloped, and premature convergence to suboptimal small time steps. Our Pretrain-Adapt

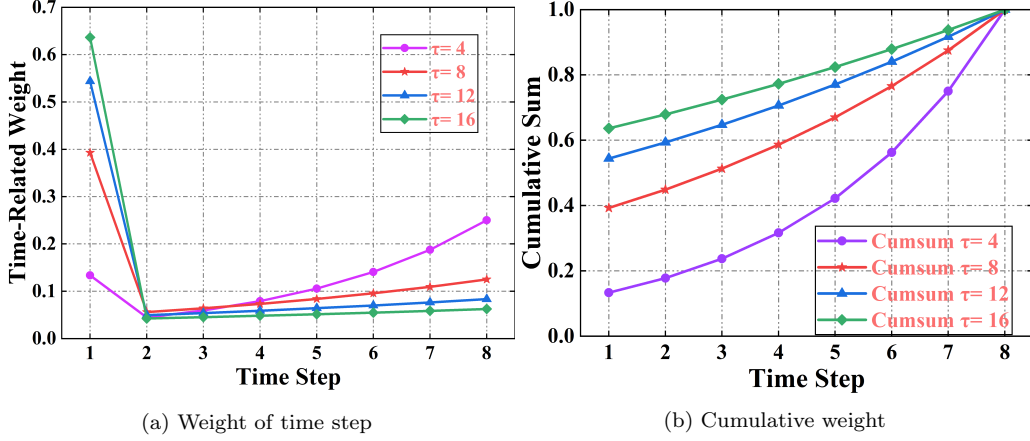


Figure 3: The weights corresponding to different time steps (a) and the cumulative weights (b) under the hybrid input mode. (a) reflects the weights of the outputs at different time steps contributing to the total output, while (b) highlights the sum of the weight percentages of the current and previous time steps’ contributions to the total output. The lower the weights of the time steps closer to the maximum time step, the less significant the outputs at these time steps are, and truncating these outputs would have a lesser impact on the performance.

Time-step Adjustment (PATA) framework addresses these through a structured two-phase approach (Figure 2b). The first phase focuses on pretraining, where the model learns stable representations using the full  $T$  time steps with rendering loss  $\mathcal{L}_{\text{Render}}(T)$ . The subsequent adaptation phase introduces the trainable time step  $t^*$ , optimized through three key components: (1) adversarial loss  $\mathcal{L}_{\text{adv}}$  for time-step adjustment, (2) rendering loss  $\mathcal{L}_{\text{Render}}(t_r^*)$  evaluated at the adapted step  $t_r^*$ , and (3) distillation loss  $\mathcal{L}_{\text{distill}}$  that exploits the known performance hierarchy across time steps [24, 42, 45]. This phased strategy ensures stable training while achieving content-aware time-step reduction.

#### 4.3.2. Initial Stage Training

The initial training phase establishes a robust pre-trained model for subsequent time-step optimization. We employ a composite loss function com-

prising three key components:

$$\mathcal{L}_{\text{Render}}(T) = M_T + \mathcal{L}_{\text{consis}}(T) + \mathcal{L}_{\text{Cauchy}} \quad (13)$$

$$\mathcal{L}_{\text{consis}}(T) = \gamma_0 \|C_T - \text{gt}\|_2 + \gamma_1 \left( 1 - \frac{C_T \cdot \text{gt}}{\|C_T\| \|\text{gt}\| + \epsilon} \right) \quad (14)$$

$$\mathcal{L}_{\text{Cauchy}} = \gamma_2 \sum_i \log(1 + 2\sigma_i) \quad (15)$$

where  $M_T$  denotes the Mean Squared Error between the rendered color  $C_T$  (computed via Equation 4) and ground truth  $\text{gt}$ . The consistency loss  $\mathcal{L}_{\text{consis}}(T)$  combines L2 distance and cosine similarity to enforce both magnitude and directional alignment between rendered and ground truth images. Following [30], the Cauchy regularization term  $\mathcal{L}_{\text{Cauchy}}$  promotes sparsity in the density predictions  $\sigma_i$ . The coefficients  $\gamma_0$ ,  $\gamma_1$ , and  $\gamma_2$  balance these loss components during optimization, which we set to  $5e^{-5}$ ,  $5e^{-2}$ , and  $1e^{-6}$ , respectively.

#### 4.3.3. Adversarial Training Loss

Following the initial training phase, we activate the trainable target time step  $t^*$  as defined in Equation (12). While our hybrid input mode enables control over time-step contributions through the decay parameter  $\tau$ , excessive  $\tau$  values hinder effective training by limiting input information propagation (Equation (10)). To address this, we introduce an adversarial loss:

$$\mathcal{L}_{\text{adv}} = \alpha \mathcal{L}_{\text{extra}} + \beta \mathcal{L}_{\text{penalty}} \quad (16)$$

Here  $\alpha$  and  $\beta$  are hyperparameters. The first component  $\mathcal{L}_{\text{extra}}$  regulates both  $\tau$  and  $t^*$  through:

$$\mathcal{L}_{\text{extra}} = \frac{\|w_{i,t>t_r^*}\|_2}{\|W_{\text{points}}\|_2} + \frac{\|c_{t>t_r^*}\|_2}{\|C_T\|_2} + e^\tau \quad (17)$$

Where  $w_{i,t>t_r^*}$  represents weights for time steps beyond  $t_r^*$ ,  $W_{\text{points}}$  denotes sampling point weights from Equation (3),  $c_{t>t_r^*}$  is the weighted output for excess time steps, and  $C_T$  is the final rendered color from Equation (4). The exponential term  $e^\tau$  prevents excessive growth of  $\tau$ . To counterbalance  $\mathcal{L}_{\text{extra}}$ 's tendency to increase  $t^*$ , we introduce a penalty term:

$$\mathcal{L}_{\text{penalty}} = (M_T \cdot M_{t_r^*}^{-1})_{\text{item}} e^{t^*} \quad (18)$$



The performance ratio ( $M_T \cdot M_{t_r^*}^{-1}$ ) dynamically scales the penalty based on rendering quality at  $t_r^*$  relative to  $T$ , where the subscript indicates this operates as a numerical coefficient without affecting gradient computation. The hyperparameter  $\beta$  in Equation (16) provides explicit control over the target time-step range for different application requirements, and  $\alpha$  is set as  $1e^{-6}$  in the experiments.

#### 4.3.4. Dynamic Time-step Training

While Equation (18) effectively links model performance to  $t^*$ , the rounding operation required to obtain  $t_r^*$  introduces training instability. When  $t^*$  fluctuates near integer midpoints (e.g., 0.5),  $t_r^*$  exhibits discontinuous jumps that disrupt both the loss landscape and the performance metric  $M_{t_r^*}^{-1}$  in Equation (18). To mitigate this, we introduce a smoothing strategy applied to both Equation (13) and Equation (18):

$$M_{t_r^*, \text{smooth}} = \begin{cases} M_{t_r^*}(1 + t^* - t_r^*) + M_{t_r^*-1}(t_r^* - t^*) & t_c^* = t_r^* \\ M_{t_r^*}(t_c^* - t^*) + M_{t_r^*-1}(t^* - t_r^*) & t_c^* \neq t_r^* \end{cases} \quad (19)$$

where  $t_c^* = \lceil t^* \rceil$  denotes the ceiling of  $t^*$ . Building upon established SNNs knowledge [45] that higher time steps typically yield superior outputs, we employ knowledge distillation from our pre-trained model. Specifically, we compute the MSE between outputs at  $T$  and  $t_r^*$ :

$$\mathcal{L}_{\text{distill}} = \|C_T - C_{t_r^*}\|_2^2 \quad (20)$$

Note that the second training phase optimizes the output at time step  $t^*$ , while the first phase focuses on time step  $T$ . This duality enables the utilization of  $T$ 's output as a supervisory signal for  $t^*$  during the initial epochs of the second phase. As training progresses, the discrepancy between  $t^*$  and  $T$  diminishes, with Equation (20) dynamically modulating its regularization strength to enforce convergence between the two temporal outputs. The complete second-phase loss combines these components:

$$\mathcal{L} = \mathcal{L}_{\text{Render}}(t_r^*) + \mathcal{L}_{\text{adv}} + \mathcal{L}_{\text{distill}} \quad (21)$$

#### 4.4. Max Time-Step Scaling

During the initial training iterations, the inclusion of unfiltered sample points leads to substantial GPU memory consumption at each time step.

However, as training progresses, the importance sampling mechanism effectively filters out irrelevant points (those with weights below the predefined threshold), significantly reducing the active sample count [1, 32, 53]. This optimization enables stable training even with substantially increased  $T$  values while maintaining manageable memory usage. To address the memory challenges during early training, we implement a Max Time-Step Scaling strategy with two key components. First, we initialize training with a reduced  $T$  value for several epochs to prevent memory overflow during the critical sampling optimization phase. Second, once the sampling efficiency stabilizes, we restore the full  $T$  value to ensure optimal model capacity. This adaptive approach provides two significant advantages: it eliminates memory bottlenecks during initialization while maintaining full model performance, and reduces peak memory consumption by up to 69% compared to fixed- $T$  training without compromising final rendering quality.

## 5. RESULTS

### 5.1. Experimental Setup

**Datasets.** We evaluate our method on two established benchmark datasets: the Synthetic-NeRF dataset [1] and the Mip-NeRF 360 dataset [54]. The Synthetic-NeRF dataset consists of 8 synthetic scenes rendered at  $800 \times 800$  resolution, providing controlled conditions for performance analysis. For more challenging real-world scenarios, we use the Mip-NeRF 360 dataset, which features higher-resolution captures of complex natural environments with richer texture details and greater geometric complexity. This combination allows comprehensive evaluation across both synthetic and real-world conditions.

**Model.** In our experiments, we use the widely accepted INGP-NeRF framework described in Section 3.1 to validate the proposed techniques. Our implementation, built upon the *torch-ngp* framework [55], employs a density network with one hidden layer and a color network with two hidden layers, both using 128 hidden units. We fix the maximum time steps  $T = 8$  throughout training and initialize the target time step  $t^* = 7$  after the pretraining phase. All other hyperparameters remain consistent with the original INGP-NeRF implementation. Notably, our approach introduces minimal computational overhead - with shared decay factors  $\tau$  across PLIF layers, we add only 5 trainable parameters to the base model.

Table 1: Quantitative comparison under different datasets and computational loads during the inference. The data in parentheses are the proportion of energy consumption reduction relative to the original model, and the best result is highlighted in bold.

Dataset Method	Synthetic-NeRF				Mip-NeRF 360			
	PSNR $\uparrow$	SSIM $\uparrow$	Time Step $\downarrow$	Energy(mJ) $\downarrow$	PSNR $\uparrow$	SSIM $\uparrow$	Time Step $\downarrow$	Energy(mJ) $\downarrow$
INGP-NeRF	32.14	<b>0.959</b>	-	1910.54	<b>25.48</b>	<b>0.668</b>	-	$3.459 \times 1e^4$
Ours	$\beta = 1e^{-7}$	<b>32.45</b>	<b>0.959</b>	5.125	1217.99(36.25%)	25.30	0.667	$6.000 \times 1e^4$ (22.06%)
	$\beta = 5e^{-7}$	32.21	0.957	3.625	887.20(53.56%)	25.09	0.646	$4.857 \times 1e^4$ (31.46%)
	$\beta = 1e^{-6}$	32.04	0.956	2.875	779.12( <b>61.55%</b> )	25.01	0.641	$4.000 \times 1e^4$ ( <b>40.00%</b> )

**Training Detail.** The experiments are conducted using PyTorch and SpikingJelly [56] on a NVIDIA 4090 GPU with mixed precision training. In the experimental setup, we employ consistent hyperparameter configurations across both datasets. Specifically, the first stage consists of 10,000 iterations, and the second stage comprises 30,000 iterations. At the commencement of each training stage, the maximum time step  $T$  for the initial epoch is set to 2, while for the subsequent epochs, it is adjusted to 8.

Regarding the network architectures, the density network owns two fully connected layers and one PLIF layer, and the transformation of the input dimension is that the  $32 \rightarrow 128 \rightarrow 16$ . While the color network incorporates three fully connected layers and two PLIF layers, with the dimensionality transforming of  $(16 + 15) \rightarrow 128 \rightarrow 128 \rightarrow 3$ . Here, 16 represents the dimension of the viewing direction  $\mathbf{d}$ , and 15 corresponds to the dimension of the output  $\mathbf{h}$  from the density network. Both networks are succeeded by a PLIF layer with the dimensionality of 4, which is exclusively utilized for accumulating the membrane potential to generate the outputs for  $\sigma$  and  $rgb$ . For the PLIF neurons, the decay factor  $\tau$  across all PLIF layers is set to 2, and the threshold  $V_{th}$  for spike emission is set to 0.5; the hybrid input mode is adopted during the whole training process.

## 5.2. Quantitative Comparison

### 5.2.1. Experimental Results

We evaluate our method using both Peak Signal to Noise Ratio (PSNR) and Structure Similarity Index Measure (SSIM) as quantitative metrics. To analyze the performance-power trade-offs, we systematically vary the hyperparameter  $\beta$  in Equation (16), with results presented in Table 1. Our experiments reveal two key operating regimes: (1) For quality-critical applications, setting  $\beta = 1 \times 10^{-7}$  maintains rendering fidelity comparable to the original INGP-NeRF (less than 0.5 dB PSNR degradation) while still

Table 2: Comparison With Spike-Based NeRF Models on Synthetic-NeRF dataset. The best result is highlighted in bold.

Method	PSNR↑	SSIM↑	Time Step↓
Spiking-NeRF [16]	30.41	-	256
Mixed Spiking-NeRF [17]	31.61	0.949	4
SpikingNeRF-D [4]	31.64	0.952	4
SpikingNeRF-T [4]	<b>32.45</b>	0.956	<b>1</b>
Ours	32.21	<b>0.957</b>	3.625

offering energy savings. (2) For resource-constrained scenarios, increasing  $\beta$  reduces the average time steps, yielding significant power reduction (up to 61.55% savings) with adjustable quality trade-offs. This flexible operating range enables deployment across diverse application requirements, from high-end visualization to edge devices with strict power budgets.

### 5.2.2. Comparative Study

We evaluate our model’s performance at  $\beta = 5 \times 10^{-7}$  against other NeRF-based approaches, analyzing both rendering quality and required time steps. As no other spike-based NeRF models have been evaluated on the MipNeRF360 dataset to date, we restrict our comparisons to the Synthetic-NeRF dataset. Table 2 presents comparative results on the Synthetic-NeRF dataset, demonstrating that our method achieves superior rendering quality with fewer time steps than most spike-based alternatives. The exception is SpikingNeRF-T [4], which modifies TensorRF for SNNs compatibility through input dimension adjustments and zero-padding to maintain consistent sampling points per ray. While effective, these architectural changes incur a 0.69 dB PSNR penalty relative to the original TensorRF. Notably, our approach preserves INGP-NeRF’s original input/output dimensions while maintaining comparable PSNR to the ANN version (less than 0.5 dB difference). This demonstrates our method’s stronger learning capacity and more efficient spiking adaptation, achieving high-quality rendering without structural modifications to the base architecture.

We further evaluate our approach against conventional ANN-based methods, with comparative results presented in Table 3. On synthetic scenes, our method achieves comparable rendering quality to ANNs in both PSNR and SSIM metrics, demonstrating its ability to maintain high visual fidelity. For

complex real-world scenes, our approach not only preserves superior energy efficiency but also surpasses several ANN implementations in PSNR performance. This dual advantage of competitive rendering quality and enhanced energy efficiency highlights the practical value of our method for both synthetic and real-world applications.

Table 3: Comparison With The Other NeRF-based Methods. The best results on each dataset are shown in bold.

Synthetic-NeRF			MipNeRF-360		
Method	PSNR $\uparrow$	SSIM $\uparrow$	Method	PSNR $\uparrow$	SSIM $\uparrow$
JaxNeRF[57]	31.65	0.952	NeRF[1]	23.85	0.605
MipNeRF[3]	33.09	0.961	NeRF++[58]	25.11	0.676
TensoRF[53]	<b>33.14</b>	<b>0.963</b>	MipNeRF[3]	24.04	0.616
INGP[32]	32.14	0.959	INGP[32]	25.48	0.668
SRes[59]	32.52	0.959	Nerfacto[60]	26.39	0.731
BiRF[30]	32.64	0.958	ZipNeRF[61]	<b>28.54</b>	<b>0.828</b>
Ours	32.21	0.957	Ours	25.09	0.646

### 5.2.3. Energy Efficiency Analysis

Table 4: Computation workload for rendering an  $800 \times 800$  image. The best result is highlighted in bold.

Method	Params $\downarrow$	Network	FLOPs(G) $\downarrow$	SOPs(G) $\downarrow$	Energy(mJ) $\downarrow$
SpikingNeRF-D[4]	57.74M	39-128-128-3	<b>31.108</b>	79.388	<b>214.55</b>
SpikingNeRF-T[4]	17.55M	150-128-128-3	304.968	<b>64.276</b>	1460.70
ours	<b>12.22M</b>	32-128-16 31-128-128-3	171.698	108.208	887.20

We conduct a comprehensive comparison of energy efficiency between PATA and the original INGP framework for single-image rendering, with results detailed in Table 1. Since INGP’s color network depends partially on the density network’s output, our time-step reduction strategy inherently decreases computational complexity (FLOPs). Following established methodologies [4, 62], we measure the inference power consumption at 45nm

technology:

$$SOPs = fr \times T \times Flops \quad (22)$$

$$Energy_{SOPs} = 0.9pJ \times SOP_s \quad (23)$$

$$Energy_{FLOPs} = 4.6pJ \times FLOPs \quad (24)$$

$$Energy_{total} = Energy_{SOPs} + Energy_{FLOPs} \quad (25)$$

Where  $SOPs$  denotes the number of spike-based operations,  $FLOPs$  means the flop-point operations. The energy costs of a single spike-based operation and a single floating-point operation are  $0.9pJ$  and  $4.6pJ$ , respectively. In Table 1 we report the energy consumption of rendering a single image under different datasets and different experimental parameter settings, showing that PATA can achieve up to **61.55%** energy consumption reduction while maintaining near-identical rendering quality ( $<0.5$  dB PSNR degradation). This significant efficiency gain underscores PATA’s practicality for deployment in resource-constrained scenarios without compromising visual fidelity.

We obtained the runtime power consumption of the work in [4] by reproducing its open-source code, with the results presented in Table 4. Although SpikingNeRF-D employs a coarse-to-fine strategy during inference to minimize the number of sampled points and thereby reduce computational energy consumption, it suffers from significant storage overhead due to its large number of parameters. Additionally, there exists a notable gap in rendering quality between SpikingNeRF-D and both SpikingNeRF-T and our proposed scheme. For SpikingNeRF-T, although it yields the highest PSNR, its power consumption is considerably higher than that of other models. In contrast, our scheme features fewer parameters and can achieve a more flexible trade-off between energy consumption and quantization metrics.

### 5.3. Qualitative Results

Figure 4 compares the rendering performance of the original INGP-NeRF and our PATA framework at varying target time steps. The results demonstrate that PATA maintains comparable visual quality to INGP-NeRF even when reducing time steps by 50%. We also provide visual comparisons of different spike-based NeRF models and their ANN prototypes under the same scenarios, as shown in Figure 5. For relatively complex scenarios, our approach can better ensure the rendering quality of texture details. For instance, in the drums scenario, other methods exhibit varying degrees of distortion when rendering the surfaces of the drums, whereas our approach

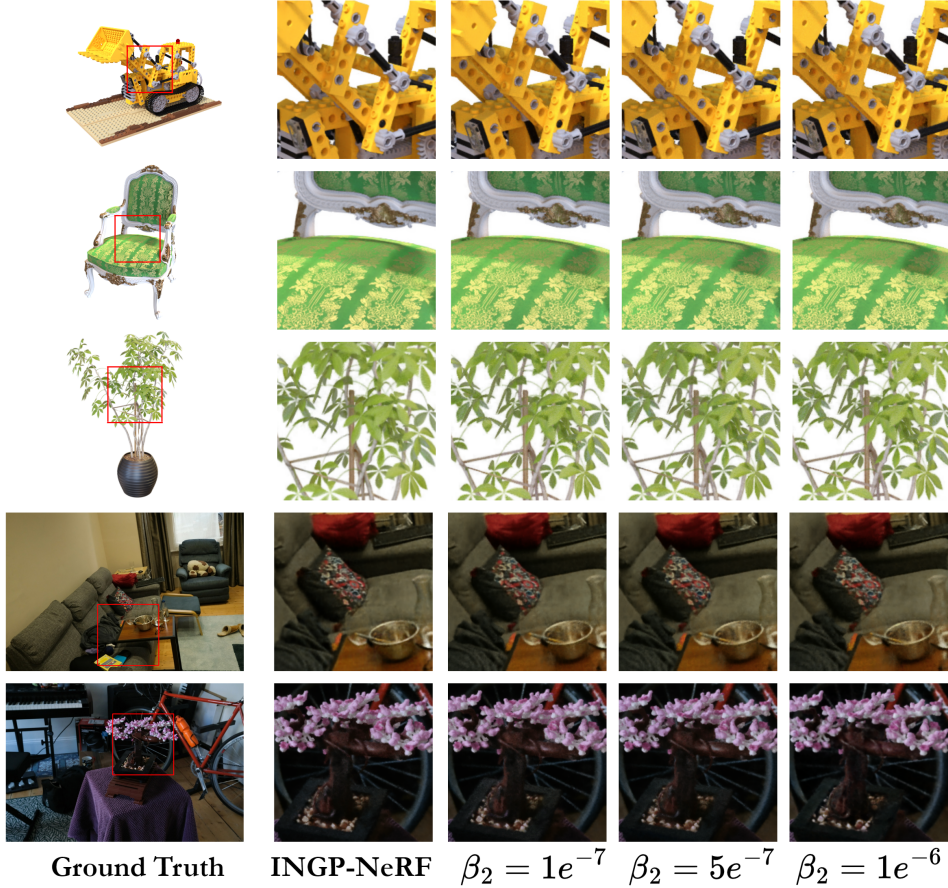


Figure 4: **Qualitative results** for the lego, chair, and ficus scenes from the Synthetic-NeRF dataset, as well as the room and bonsai scenes from the MipNeRF360 dataset. The render quality is comparable to that of INGP-NeRF across various  $t_r^*$ .

presents much clearer results. Figure 6 further analyzes the correlation between scene complexity and optimal time steps  $t^*$ . Across both datasets, we observe a consistent inverse relationship between  $t^*$  and PSNR: scenes with simpler textures (e.g., chair, hotdog, room) achieve high-quality rendering with only 3–4 time steps, while complex objects (e.g., drums, bicycle) require significantly more time steps to preserve fine details. This adaptive behavior confirms that PATA automatically allocates computational resources according to scene complexity. More importantly, our approach introduces a key innovation by enabling scene-adaptive time-step optimization within a unified training framework. Unlike prior dynamic time-step methods that



Figure 5: **Qualitative comparison** of rendering results for different models in drums, ship, and materials scenes. PATA can provide more clear rendering details compared to other models.

rely on confidence thresholds [46] or reinforcement learning [47], our method maintains GPU-friendly parallelism during inference by applying consistent time steps across all sampling points within a scene. This architectural advantage ensures efficient hardware utilization while preserving the ability to tailor computation to each scene’s complexity.

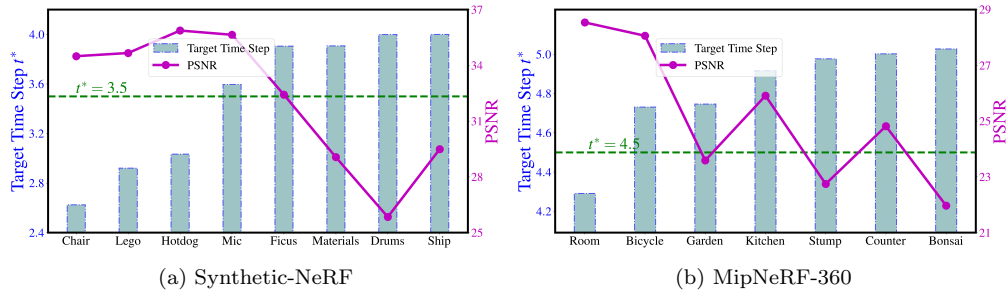


Figure 6: Relationship between PSNR and target time steps for different scenes.

#### 5.4. Ablation Study

We perform comprehensive ablation studies on the Synthetic-NeRF dataset to validate our framework’s design choices. Our experiments focus on three key configurations: 1) **Baseline**: Training exclusively with the initial phase



(full  $T$  time steps) for the combined duration of both phases, establishing our reference performance. 2) **Full PATA**: Our complete two-phase approach combining pretraining and dynamic time-step adaptation. 3) **Direct Adaptation**: Training with dynamic time steps from initialization, omitting the pretraining phase.

Table 5: Ablation study of different decay modes during training. The best result is highlighted in bold.

Method	PSNR $\uparrow$	SSIM $\uparrow$	Time Step $\downarrow$
Decay	31.82	0.955	8.000
No-Decay	32.09	0.956	8.000
Baseline	<b>32.12</b>	<b>0.957</b>	8.000

We first validated the effectiveness of the proposed hybrid input mode. As presented in Table 5, the performance was the poorest when only the decay mode was employed. The underlying reason lies in that the input at each time step is scaled by  $1/\tau$ , which reduces the magnitude of the accumulated membrane potential and thereby impairs the model’s performance. This phenomenon becomes increasingly prominent as the time steps decrease. When adopting the non-decay mode solely, in contrast to the decay mode, since an exponential operation is performed first at each time step before accumulating the membrane potential, the value of the membrane potential is likely to overflow. Nevertheless, benefiting from the regularity provided by Formula(14) during training, which reduces the overall discrepancy between the accumulated membrane potential and the ground truth, its PSNR is slightly lower compared to the hybrid input scheme. The hybrid input mode demonstrates advantages over the other two decay modes. Furthermore, it can adjust the value of  $\tau$  to dynamically regulate the output weights at different time steps, exhibiting more extensive application potential.

To highlight the importance of the two-stage training, we present the model performances under three configurations in Table 6. PATA achieves superior rendering quality (PSNR) while reducing time steps by 55% compared to the baseline. The direct adaptation approach converges to similar time-step reductions but suffers a 0.53 dB PSNR degradation, demonstrating that our pretraining phase is crucial for learning robust temporal representations. These results confirm that our optimized framework better integrates temporal information and maintains stronger learning capability even with

varying inference time steps.

Table 6: Ablation study of two-stage training. The best result is highlighted in bold.

Method	PSNR $\uparrow$	SSIM $\uparrow$	Time Step $\downarrow$
Baseline	32.12	<b>0.957</b>	8.000
w/o pretrain	31.59	0.954	<b>3.625</b>
Ours	<b>32.21</b>	<b>0.957</b>	<b>3.625</b>

Table 7: Ablation study on the adversarial loss:  $\mathcal{L}_{\text{extra}}$ ,  $\mathcal{L}_{\text{penalty}}$  and  $\mathcal{L}_{\text{adv}}$ . The best result is highlighted in bold.

Method	PSNR $\uparrow$	SSIM $\uparrow$	Time Step $\downarrow$
w/o $\mathcal{L}_{\text{extra}}$	31.69	0.953	<b>1.625</b>
w/o $\mathcal{L}_{\text{penalty}}$	<b>32.61</b>	<b>0.960</b>	6.625
w/o $\mathcal{L}_{\text{adv}}$	32.02	0.957	5.875
Ours	32.21	0.957	3.625

We also systematically evaluate the role of  $\mathcal{L}_{\text{adv}}$  in balancing time-step reduction and rendering quality (Table 7). The adversarial loss combines two competing objectives:  $\mathcal{L}_{\text{extra}}$  for quality preservation through  $\tau$  and  $t^*$  regulation, and  $\mathcal{L}_{\text{penalty}}$  for time-step reduction. Three key experimental configurations reveal distinct behaviors. First, ablation of  $\mathcal{L}_{\text{extra}}$  drives  $t_r^*$  to minimal values (1.625) but incurs a significant PSNR penalty ( $\sim 0.52$  dB) due to unconstrained time-step reduction. Second, removal of  $\mathcal{L}_{\text{penalty}}$  improves PSNR by 0.4 dB but increases time steps by  $1.5\times$ , eliminating energy benefits. Third, complete omission of  $\mathcal{L}_{\text{adv}}$  produces marginally reduced  $t_r^*$  but severely degrades PSNR ( $\sim 0.19$  dB). Our complete method achieves the optimal balance, reducing  $t_r^*$  by 55% while maintaining PSNR. These results demonstrate that joint optimization of both loss components is essential for simultaneously achieving efficiency and rendering quality.

## 6. CONCLUSION

In this work, we present PATA, a novel framework that dynamically adapts time-step allocation to scene complexity for neural rendering tasks, achieving an optimal trade-off between rendering quality and computational

efficiency. Our approach introduces three key innovations. First, the hybrid input mode strategically combines existing neuron input modes to regulate the decay factor  $\tau$ , effectively reducing the influence of later time steps on the final output. Second, the two-stage training strategy establishes robust scene representations before optimizing parameterized time steps via adversarial loss, enabling content-aware computation. Third, the smoothed MSE loss stabilizes training during dynamic time-step adjustments. Experimental results demonstrate that PATA successfully adapts time-step allocation to both scene content and application constraints, maintaining rendering fidelity while significantly reducing dynamic energy consumption during inference compared to conventional approaches.

## References

- [1] B. Mildenhall, P. P. Srinivasan, M. Tancik, J. T. Barron, R. Ramamoorthi, R. Ng, Nerf: Representing scenes as neural radiance fields for view synthesis, *Communications of the ACM* 65 (1) (2021) 99–106.
- [2] H. Zhu, T. He, X. Li, B. Li, Z. Chen, Is vanilla mlp in neural radiance field enough for few-shot view synthesis?, in: *Proceedings of the IEEE/CVF Conference on Computer Vision and Pattern Recognition*, 2024, pp. 20288–20298.
- [3] J. T. Barron, B. Mildenhall, M. Tancik, P. Hedman, R. Martin-Brualla, P. P. Srinivasan, Mip-nerf: A multiscale representation for anti-aliasing neural radiance fields, in: *Proceedings of the IEEE/CVF international conference on computer vision*, 2021, pp. 5855–5864.
- [4] X. Yao, Q. Hu, T. Liu, Z. Mo, Z. Zhu, Z. Zhuge, J. Cheng, Spikingnerf: Making bio-inspired neural networks see through the real world, *arXiv preprint arXiv:2309.10987* (2023).
- [5] W. Liu, X. X. Zheng, J. Yu, X. Lou, Content-aware radiance fields: Aligning model complexity with scene intricacy through learned bitwidth quantization, in: *European Conference on Computer Vision*, Springer, 2024, pp. 239–256.
- [6] X. Zhang, Y. Wang, S. Fang, Z. Wang, H. Zhang, D. Qi, W. Ding, Asf-nerf: Large-scale scene rendering with adaptive sampling and feature-aware compression, in: *ICASSP 2025-2025 IEEE International Confer-*

- ence on Acoustics, Speech and Signal Processing (ICASSP), IEEE, 2025, pp. 1–5.
- [7] X. Xie, R. Gherardi, Z. Pan, S. Huang, Hollownerf: Pruning hashgrid-based nerfs with trainable collision mitigation, in: Proceedings of the IEEE/CVF International Conference on Computer Vision, 2023, pp. 3480–3490.
  - [8] A. Hasssan, A. Anupreetham, J. Meng, J.-s. Seo, Quant-nerf: Efficient end-to-end quantization of neural radiance fields with low-precision 3d gaussian representation, in: ICASSP 2025-2025 IEEE International Conference on Acoustics, Speech and Signal Processing (ICASSP), IEEE, 2025, pp. 1–5.
  - [9] K. Zhou, Y. Qiu, Y. Li, Q. Zhao, G. Zhou, Gradient aware adaptive quantization: Locally uniform quantization with learnable clipping thresholds for globally non-uniform weights, *Neural Networks* (2025) 107778.
  - [10] T. Wang, B. Dong, K. Zhang, J. Li, L. Xu, Slim-rffnet: Slim deep convolution random fourier feature network for image classification, *Knowledge-Based Systems* 237 (2022) 107878.
  - [11] T. Chen, S. Duan, L. Wang, Exploiting memristive autapse and temporal distillation for training spiking neural networks, *Knowledge-Based Systems* 305 (2024) 112627.
  - [12] S. Yan, J. Fei, H. Wei, B. Zhao, Z. Wang, G. Yang, Adversarial event patch for spiking neural networks, *Knowledge-Based Systems* 309 (2025) 112865.
  - [13] A. Tavanaei, M. Ghodrati, S. R. Kheradpisheh, T. Masquelier, A. Maida, Deep learning in spiking neural networks, *Neural networks* 111 (2019) 47–63.
  - [14] N. Rathi, I. Chakraborty, A. Kosta, A. Sengupta, A. Ankit, P. Panda, K. Roy, Exploring neuromorphic computing based on spiking neural networks: Algorithms to hardware, *ACM Computing Surveys* 55 (12) (2023) 1–49.

- [15] Z. Liao, Y. Liu, Q. Zheng, G. Pan, Spiking nerf: Representing the real-world geometry by a discontinuous representation, in: Proceedings of the AAAI Conference on Artificial Intelligence, Vol. 38, 2024, pp. 13790–13798.
- [16] Z. Li, Y. Ma, J. Zhou, P. Zhou, Spiking-nerf: Spiking neural network for energy-efficient neural rendering, *ACM Journal on Emerging Technologies in Computing Systems* 20 (3) (2025) 1–23.
- [17] K. Wang, L. Zou, Mixed spiking nerf: Towards a more efficient neural radiance fields, in: ICASSP 2025-2025 IEEE International Conference on Acoustics, Speech and Signal Processing (ICASSP), IEEE, 2025, pp. 1–5.
- [18] Y. Gu, Z. Wang, D. Ye, R. Xu, Sharpening your density fields: Spiking neuron aided fast geometry learning, *arXiv preprint arXiv:2412.09881* (2024).
- [19] Y. Guo, Y. Bai, L. Hu, M. Liu, Z. Guo, L. Ma, T. Huang, Spike-nerf: Neural radiance field based on spike camera, in: 2024 IEEE International Conference on Multimedia and Expo (ICME), IEEE, 2024, pp. 1–6.
- [20] T. Takikawa, A. Evans, J. Tremblay, T. Müller, M. McGuire, A. Jacobson, S. Fidler, Variable bitrate neural fields, in: *ACM SIGGRAPH 2022 Conference Proceedings*, 2022, pp. 1–9.
- [21] S. Girish, A. Shrivastava, K. Gupta, Shacira: Scalable hash-grid compression for implicit neural representations, in: *Proceedings of the IEEE/CVF International Conference on Computer Vision*, 2023, pp. 17513–17524.
- [22] G.-W. Yang, W.-Y. Zhou, H.-Y. Peng, D. Liang, T.-J. Mu, S.-M. Hu, Recursive-nerf: An efficient and dynamically growing nerf, *IEEE Transactions on Visualization and Computer Graphics* 29 (12) (2022) 5124–5136.
- [23] G. Datta, P. A. Beerel, Can deep neural networks be converted to ultra low-latency spiking neural networks?, in: 2022 Design, Automation & Test in Europe Conference & Exhibition (DATE), IEEE, 2022, pp. 718–723.

- [24] Y. Kim, Y. Li, H. Park, Y. Venkatesha, A. Hambitzer, P. Panda, Exploring temporal information dynamics in spiking neural networks, in: Proceedings of the AAAI Conference on Artificial Intelligence, Vol. 37, 2023, pp. 8308–8316.
- [25] B. Li, L. Leng, S. Shen, K. Zhang, J. Zhang, J. Liao, R. Cheng, Efficient deep spiking multilayer perceptrons with multiplication-free inference, IEEE Transactions on Neural Networks and Learning Systems (2024).
- [26] Q. Ai, Y. Yang, M. Cai, K. Chen, Q. Liu, L. Ma, A cross-layer residual spiking neural network with adaptive threshold leaky integrate-and-fire neuron and learnable surrogate gradient, Knowledge-Based Systems (2025) 113575.
- [27] A. Stanojevic, S. Woźniak, G. Bellec, G. Cherubini, A. Pantazi, W. Gerstner, High-performance deep spiking neural networks with 0.3 spikes per neuron, Nature Communications 15 (1) (2024) 6793.
- [28] F. Liu, W. Zhao, Z. Wang, Y. Chen, T. Yang, Z. He, X. Yang, L. Jiang, Sato: spiking neural network acceleration via temporal-oriented dataflow and architecture, in: Proceedings of the 59th ACM/IEEE Design Automation Conference, 2022, pp. 1105–1110.
- [29] W. Fang, Z. Yu, Z. Zhou, D. Chen, Y. Chen, Z. Ma, T. Masquelier, Y. Tian, Parallel spiking neurons with high efficiency and ability to learn long-term dependencies, Advances in Neural Information Processing Systems 36 (2023) 53674–53687.
- [30] S. Shin, J. Park, Binary radiance fields, Advances in neural information processing systems 36 (2023) 55919–55931.
- [31] C. Reiser, S. Garbin, P. Srinivasan, D. Verbin, R. Szeliski, B. Mildenhall, J. Barron, P. Hedman, A. Geiger, Binary opacity grids: Capturing fine geometric detail for mesh-based view synthesis, ACM Transactions on Graphics (TOG) 43 (4) (2024) 1–14.
- [32] T. Müller, A. Evans, C. Schied, A. Keller, Instant neural graphics primitives with a multiresolution hash encoding, ACM transactions on graphics (TOG) 41 (4) (2022) 1–15.

- [33] Y. Chen, Q. Wu, M. Harandi, J. Cai, How far can we compress instant-ngp-based nerf?, in: Proceedings of the IEEE/CVF Conference on Computer Vision and Pattern Recognition, 2024, pp. 20321–20330.
- [34] L. Jiang, L. Wang, G-nelf: Memory-and data-efficient hybrid neural light field for novel view synthesis, arXiv preprint arXiv:2409.05617 (2024).
- [35] Y. Wu, L. Deng, G. Li, J. Zhu, L. Shi, Spatio-temporal backpropagation for training high-performance spiking neural networks, *Frontiers in neuroscience* 12 (2018) 331.
- [36] E. O. Neftci, H. Mostafa, F. Zenke, Surrogate gradient learning in spiking neural networks: Bringing the power of gradient-based optimization to spiking neural networks, *IEEE Signal Processing Magazine* 36 (6) (2019) 51–63.
- [37] X. Yao, F. Li, Z. Mo, J. Cheng, Glif: A unified gated leaky integrate-and-fire neuron for spiking neural networks, *Advances in Neural Information Processing Systems* 35 (2022) 32160–32171.
- [38] B. Yin, F. Corradi, S. M. Bohté, Accurate and efficient time-domain classification with adaptive spiking recurrent neural networks, *Nature Machine Intelligence* 3 (10) (2021) 905–913.
- [39] S. Lian, J. Shen, Z. Wang, H. Tang, Im-lif: Improved neuronal dynamics with attention mechanism for direct training deep spiking neural network, *IEEE Transactions on Emerging Topics in Computational Intelligence* 8 (2) (2024) 2075–2085.
- [40] T. Zhang, K. Yu, J. Zhang, H. Wang, Da-lif: Dual adaptive leaky integrate-and-fire model for deep spiking neural networks, in: ICASSP 2025-2025 IEEE International Conference on Acoustics, Speech and Signal Processing (ICASSP), IEEE, 2025, pp. 1–5.
- [41] S. Deng, Y. Li, S. Zhang, S. Gu, Temporal efficient training of spiking neural network via gradient re-weighting, arXiv preprint arXiv:2202.11946 (2022).
- [42] C. Yu, X. Zhao, L. Liu, S. Yang, G. Wang, E. Li, A. Wang, Efficient distillation of deep spiking neural networks for full-range timestep deployment, arXiv preprint arXiv:2501.15925 (2025).

- [43] Y. Yan, H. Chu, Y. Jin, Y. Huan, Z. Zou, L. Zheng, Backpropagation with sparsity regularization for spiking neural network learning, *Frontiers in Neuroscience* 16 (2022) 760298.
- [44] F. Liu, H. Li, N. Yang, Z. Wang, T. Yang, L. Jiang, Teas: Exploiting spiking activity for temporal-wise adaptive spiking neural networks, in: 2024 29th Asia and South Pacific Design Automation Conference (ASP-DAC), IEEE, 2024, pp. 842–847.
- [45] L. Zuo, Y. Ding, M. Jing, K. Yang, Y. Yu, Self-distillation learning based on temporal-spatial consistency for spiking neural networks, *arXiv preprint arXiv:2406.07862* (2024).
- [46] C. Li, E. G. Jones, S. Furber, Unleashing the potential of spiking neural networks with dynamic confidence, in: *Proceedings of the IEEE/CVF International Conference on Computer Vision*, 2023, pp. 13350–13360.
- [47] Y. Li, T. Geller, Y. Kim, P. Panda, Seenn: towards temporal spiking early exit neural networks, *Advances in Neural Information Processing Systems* 36 (2023) 63327–63342.
- [48] Y. Li, A. Moitra, T. Geller, P. Panda, Input-aware dynamic timestep spiking neural networks for efficient in-memory computing, in: 2023 60th ACM/IEEE Design Automation Conference (DAC), IEEE, 2023, pp. 1–6.
- [49] X. Zhong, S. Hu, W. Liu, W. Huang, J. Ding, Z. Yu, T. Huang, Towards low-latency event-based visual recognition with hybrid step-wise distillation spiking neural networks, in: *Proceedings of the 32nd ACM International Conference on Multimedia*, 2024, pp. 9828–9836.
- [50] S. Zhang, Q. Yang, C. Ma, J. Wu, H. Li, K. C. Tan, Tc-lif: A two-compartment spiking neuron model for long-term sequential modelling, in: *Proceedings of the AAAI conference on artificial intelligence*, Vol. 38, 2024, pp. 16838–16847.
- [51] W. Fang, Y. Chen, J. Ding, Z. Yu, T. Masquelier, D. Chen, L. Huang, H. Zhou, G. Li, Y. Tian, Spikingjelly: An open-source machine learning infrastructure platform for spike-based intelligence, *Science Advances* 9 (40) (2023) eadi1480.



- [52] W. Fang, Z. Yu, Y. Chen, T. Masquelier, T. Huang, Y. Tian, Incorporating learnable membrane time constant to enhance learning of spiking neural networks, in: Proceedings of the IEEE/CVF International Conference on Computer Vision (ICCV), 2021, pp. 2661–2671.
- [53] A. Chen, Z. Xu, A. Geiger, J. Yu, H. Su, Tensorf: Tensorial radiance fields, in: European conference on computer vision, Springer, 2022, pp. 333–350.
- [54] J. T. Barron, B. Mildenhall, D. Verbin, P. P. Srinivasan, P. Hedman, Mip-nerf 360: Unbounded anti-aliased neural radiance fields, in: Proceedings of the IEEE/CVF conference on computer vision and pattern recognition, 2022, pp. 5470–5479.
- [55] J. Tang, Torch-ngp: a pytorch implementation of instant-ngp, <https://github.com/ashawkey/torch-ngp> (2022).
- [56] W. Fang, Y. Chen, J. Ding, Z. Yu, T. Masquelier, D. Chen, L. Huang, H. Zhou, G. Li, Y. Tian, Spikingjelly: An open-source machine learning infrastructure platform for spike-based intelligence, Science Advances 9 (40) (2023) eadi1480. arXiv:<https://www.science.org/doi/pdf/10.1126/sciadv.adi1480>, doi:10.1126/sciadv.adi1480. URL <https://www.science.org/doi/abs/10.1126/sciadv.adi1480>
- [57] B. Deng, J. T. Barron, P. P. Srinivasan, JaxNeRF: an efficient JAX implementation of NeRF (2020). URL <https://github.com/google-research/google-research/tree/master/jaxnerf>
- [58] K. Zhang, G. Riegler, N. Snavely, V. Koltun, Nerf++: Analyzing and improving neural radiance fields, arXiv preprint arXiv:2010.07492 (2020).
- [59] S. Dai, Y. Cao, P. Duan, X. Chen, Sres-nerf: improved neural radiance fields for realism and accuracy of specular reflections, in: International Conference on Multimedia Modeling, Springer, 2023, pp. 306–317.
- [60] M. Tancik, E. Weber, E. Ng, R. Li, B. Yi, T. Wang, A. Kristoffersen, J. Austin, K. Salahi, A. Ahuja, et al., Nerfstudio: A modular framework for neural radiance field development, in: ACM SIGGRAPH 2023 conference proceedings, 2023, pp. 1–12.

- [61] J. T. Barron, B. Mildenhall, D. Verbin, P. P. Srinivasan, P. Hedman, Zip-nerf: Anti-aliased grid-based neural radiance fields, in: Proceedings of the IEEE/CVF International Conference on Computer Vision, 2023, pp. 19697–19705.
- [62] X. Shi, Z. Hao, Z. Yu, Spikingresformer: bridging resnet and vision transformer in spiking neural networks, in: Proceedings of the IEEE/CVF Conference on Computer Vision and Pattern Recognition, 2024, pp. 5610–5619.